

A scenario for ultra-diffuse satellite galaxies with low velocity dispersions: the case of [KKS 2000]04

ADI NUSSER¹

¹*Department of Physics and the Asher Space Research Institute, Israel Institute of Technology Technion, Haifa 32000, Israel
and
Guangdong Technion-Israel Institute of Technology, Shantou 515063, P.R.China*

ABSTRACT

A scenario for achieving a low velocity dispersion for the galaxy [KKS 2000]04 (aka NGC 1052-DF2) and similar galaxies is presented. A progenitor halo corresponding to a $z = 0$ halo of mass $\lesssim 5 \times 10^{10} M_{\odot}$ and a low concentration parameter (but consistent with cosmological simulations) infalls onto a Milky Way-size host at early times. Substantial removal of cold gas from the inner regions by supernova feedback and ram pressure, assisted by tidal stripping of the dark matter in the outer regions, leads to a substantial reduction of the velocity dispersion of stars within one effective radius. In this framework, the observed stellar content of [KKS 2000]04 is associated with a progenitor mass close to that inferred from the global stellar-to-halo-mass ratio. As far as the implications of kinematics are concerned, even if at a ~ 20 Mpc distance, it is argued that [KKS 2000]04 is no more peculiar than numerous early type galaxies with seemingly little total dark-matter content.

Keywords: galaxies: halos - cosmology: theory, dark matter, galaxies

1. INTRODUCTION

Dark matter (DM) is subdominant within the effective radii (enclosing half the total light) R_e of ordinary early type galaxies (ETG; see Cappellari 2016, for a review). The inferred average DM fraction within R_e is $\sim 30\%$, and a fraction of these galaxies remains consistent without any DM in the inner regions. These findings are obtained using analyses of the stellar kinematics as well as gravitational lensing (e.g. Treu & Koopmans 2004; Mamon & Łokas 2005a; Auger et al. 2009; Thomas et al. 2011). Outer parts of ETGs extending to several R_e could be directly probed with the kinematical measurements of planetary nebulae (PN) that are detectable through strong emission lines. While it is reasonable that the stellar kinematics in the inner regions is only mildly dominated by DM, a puzzle emerged when galaxies with PN kinematics required very little DM also in the outer regions (Romanowsky et al. 2003). However, a high DM content has been demonstrated to reproduce the observed low velocity dispersion of PNs in a realistic scenario for the formation of ETGs, where the PNs are expected to follow elongated orbits (Dekel, et al. 2005).

The global stellar-to-halo-mass ratio (SHMR; Behroozi et al. 2010; Moster et al. 2013; Rodríguez-Puebla et al. 2017)

can be used to derive the peak¹ virial mass of the halo, M_h , from its observed stellar mass, M_* . Assuming DM halos with an NFW density profile (Navarro et al. 1996), the virial mass tuned to match the stellar kinematics of SDSS ellipticals yields $M_h/M_* \sim 3$ (with a large scatter) in galaxies with $M_* \sim 5 \times 10^{10} M_{\odot}$ (see figure 10 in Padmanabhan et al. 2004), a factor ~ 40 lower than the global SHMR.

Given the difficulty in inferring the virial mass from the kinematics of the inner region alone (e.g. Mamon & Łokas 2005b) and given the significant effects it can have on the DM distribution in small-mass galaxies (e.g. Pontzen & Governato 2012; Dutton et al. 2016), it is surprising that the ultra-diffuse galaxy (UDG) [KKS 2000]04 has attracted a great deal of attention as a galaxy with little DM.

The stellar velocity dispersion, σ_* , in [KKS 2000]04 has been measured separately by Emsellem et al. (2018) using the MUSE integral-field spectrograph at the (ESO) Very Large Telescope and by Danieli et al. (2019) with the Keck Cosmic Web Imager (KCWI). The velocity dispersion measurements are sufficiently different that they could lead to contrasting implications regarding the mass of the galaxy. Assuming that [KKS 2000]04 is at a distance $D = 18$ Mpc, the value $\sigma_* = 8.5_{-3.1}^{+2.3} \text{ km s}^{-1}$ derived by Danieli et al. (2019) yields a dynamical mass $M(< 1.3R_e) = (1.3 \pm$

¹ The peak halo mass is the maximum mass the halo acquires throughout its history, and it can be quite different from its current mass.

$0.8) \times 10^8 M_\odot$. However, [Emsellem et al. \(2018\)](#) obtain $\sigma_* = 10.8_{-4}^{+3.2} \text{ km s}^{-1}$, giving $M(< 1.8R_e) = 3.7_{-2.2}^{+2.5} \times 10^8$ and a factor of 1.6 smaller for $M(< R_e)$. By extrapolating the estimate $M(< 1.8R_e)$ of [Emsellem et al. \(2018\)](#) out to the virial radius using the NFW density profile, we obtain a virial mass $M_h \approx 1.4_{-1}^{+2} \times 10^9 M_\odot$ for a concentration parameter $c = 14$ and $M_h = 2.7_{-2.1}^{+5.2} \times 10^9 M_\odot$ for $c = 7$. For the stellar mass $M_* \sim 1.6 \times 10^8 M_\odot$ of [KKS 2000]04, the standard SHMR implies $M_h \sim 6 \times 10^{10} M_\odot$, significantly larger than M_h obtained by an extrapolation of $M(< 1.8R_e)$, even using the value in [Emsellem et al. \(2018\)](#). This mismatch between the SHMR and kinematical mass inference undoubtedly bears a close similarity to the situation of ETGs discussed above. In both situations and in spite of the difference in the masses, the kinematics refers to the inner regions and in both case, the prediction of the total mass falls short of the expectations. A few points should be emphasized in relation to the SHMR. The SHMR gives the peak virial mass of the progenitor throughout its entire history. For satellite galaxies, the difference between the peak and current mass can be very large (a factor of three or so) due to tidal stripping by the gravitational field of the host galaxy. Furthermore, the considered stellar mass is at the lowest end where the SHMR is not actually well constrained. Another potential caveat is that the standard SHMR may not apply to UDGs; however numerical simulations indicate that the progenitor's halos of low- and high-surface-brightness galaxies actually share main properties ([Martin et al. 2019](#)).

The current paper offers a dynamical scenario that accommodates a high M_h for the progenitor galaxy with the observed stellar kinematics of [KKS 2000]04. We extend the idea presented in [Nusser \(2019\)](#) dealing with the kinematics of 10 globular clusters (GCs) in [KKS 2000]04 ([van Dokkum et al. 2018a](#)). In addition to the stripping of the outer parts of the galaxy via external gravitational tides, the current paper explores the dynamical consequences of gas removal either via energetic feedback from supernovae or ram pressure stripping. This scenario invokes standard baryonic processes that have been demonstrated to have strong effects on the dynamics of low-mass halos (e.g. [Pontzen & Governato 2012](#); [Muratov et al. 2015](#); [Dutton et al. 2016](#)).

As in any dynamical modeling, the distance is needed to set the spatial physical scale. There are two distance estimates in the literature; [Trujillo et al. \(2019\)](#) derive a distance $D \approx 13$ Mpc, while [van Dokkum et al. \(2018b\)](#) and [Danieli, et al. \(2019\)](#), respectively, report $D = 18.7 \pm 1.7$ and $18.8_{-1.1}^{+0.9}$ Mpc. The nearer distance of 13 Mpc leads to a smaller stellar mass ($\sim 6 \times 10^7 M_\odot$) and, thus, brings [KKS 2000]04 closer to the standard SHMR ([Trujillo et al. 2019](#)). Therefore, the main interest is in the mass models for $D = 18$ Mpc, and here, we present results for this distance only.

We define the virial radius r_v to be the radius of the sphere within which the mean halo density is 200 times the critical density $\rho_c = 3H_0^2/8\pi G$. We adopt cosmological parameters based on the recent Planck collaboration ([Planck Collaboration et al. 2018](#)). Throughout this paper, we take the Hubble constant $H_0 = 67.8 \text{ km s}^{-1} \text{ Mpc}^{-1}$ and the baryonic and total mass density parameters $\Omega_b = 0.049$ and $\Omega_m = 0.311$.

The outline of the remainder of the paper is as follows. Our analysis relies on numerical simulations run under the assumption of a spherical configuration. The numerical setup and the modeled baryonic processes are described in §2. The inferred prediction for the line-of-sight (LOS) velocity dispersion and comparison with the observed dispersion is presented in §3. We conclude with a summary and a discussion in §4.

2. THE SETUP

We start with a progenitor (satellite) halo of virial mass M_h of a few times $10^{10} M_\odot$ at the outskirts of a larger parent galaxy at redshift $z \sim 2 - 3$. Since the cooling time in this halo-mass range is short compared to the dynamical time (e.g. [White & Frenk 1991](#)), we assume that a significant gas fraction has already cooled and settled well inside the virial radius. We also assume that at this stage, only a small fraction $\lesssim 0.2$ of the final stellar mass has formed ([Behroozi et al. 2013](#); [Garrison-Kimmel et al. 2019](#)). We require that most star-formation and its associated feedback occur at later stages of the evolution.

As the (gas-rich) satellite orbits into the parent halo, it begins to lose matter from its outer parts by the tidal gravitational forces of the parent halo. It also continues to form stars accompanied by supernova (SN) explosions, perhaps at a boosted rate due to tidal interactions with the host halo ([Martig & Bournaud 2008](#); [Renaud et al. 2014](#)). Because the gravitational potential depth in the satellite halos we consider corresponds to circular velocities $V_c \lesssim 60 \text{ km s}^{-1}$, SN feedback is sufficient for the removal of significant amounts of gas away from the gravitational grip of the halo ([Larson 1974](#); [Dekel & Silk 1986](#); [Munshi et al. 2013](#)). For the relevant mass range, simulations of galaxy formation ([Muratov et al. 2015](#)) indicate that the amount of gas ejected could be more than an order of magnitude larger than the mass in forming stars. In addition to star-formation feedback, another mechanism for gas removal is ram pressure exerted by the diffuse gas in the parent halo, but it is hard to estimate this effect given the little we know about the parent galaxy, especially at earlier times. Nonetheless, the UDG [KKS 2000]04 is extremely gas poor ([Chowdhury 2019](#); [Sardone et al. 2019](#)) and it is natural to assume that all of the gas that has not turned into stars has been ejected. The actual causes of gas removal are not important to our modeling, since we are only concerned with its dynamical effects.

Continuous star-formation activity could lead to slow removal of gas on time scales longer than the dynamical time of the system, while a starburst could cause a fast removal of the gas. Gas removal by ram pressure could be either or fast or slow depending on the orbital speed of the satellite and the gas density on the parent halo. In slow gas removal, the halo DM particles remain in a quasi-steady state. In contrast, in a fast ejection process, the DM particles momentarily maintain their velocities, while gaining (positive) potential energy. After a few dynamical times, the system relaxes to a new equilibrium, which, in general, is different from the steady state reached at the end of a slow gas-removal process (e.g. Pontzen & Governato 2012; Dutton et al. 2016).

At a distance $D = 18$ Mpc, [KKS 2000]04 is at a projected distance of ≈ 75 kpc from the large elliptical NGC 1052 and with a relative LOS speed of 293 km s^{-1} (van Dokkum et al. 2018a). We emphasize here that based on the measured LOS velocity dispersion in NGC 1052 ($\sim 110 \text{ km s}^{-1}$), the relative speed of [KKS 2000]04 is close to the escape velocity from NGC 1052 (see Nusser 2019) and the two galaxies, [KKS 2000]04 are likely to be just skimming each other. Still, the gravitational tides of NGC 1052 could certainly be strong enough to cause significant mass loss in [KKS 2000]04. A larger mass for NGC 1052 is obtained from the SHMR relation. The NGC 1052 stellar mass of $\sim 10^{11} M_{\odot}$ (Forbes et al. 2017), translates to a halo mass of $\sim 5 \times 10^{12} M_{\odot}$ (Wasserman et al. 2018) according to the SHMR. In any case, there is a large uncertainty in the estimation of the tidal radius of [KKS 2000]04 in the vicinity of NGC 1052 (Ogiya 2018; Wasserman et al. 2018). Nevertheless, a tidal radius of ~ 10 kpc is consistent with the observed spatial extent of the stellar component of [KKS 2000]04 and the distribution of the projected distances of its star clusters.

2.1. The Numerical Scheme

Under the assumption of a spherically symmetric configuration, we simulate the dynamical effects of cooling, stripping, and gas ejection. Only the collisionless particles are “live” and move self-consistently under the action of their own gravity as well as that of the stellar and cool-gas components. The gravitational force field of these baryonic components is computed assuming they follow the density profile of the observed stellar component but with a mass that varies with time according to the cooling and galactic wind recipes described below. Thus, the distinction between the stars and the cool gas is unimportant dynamically and, at times, we shall refer to them as accreted baryons.

Initially, the collisionless particles represent the DM and the hot gas, where the latter is assumed to follow the density distribution of the DM halo. The collisionless particles are treated as spherical shells moving under the gravitational

force field of the monopole term of the mass distribution computed relative to the halo center (as defined in the initial conditions). The self-gravity of the collisionless particles is derived following White (1983), with a force Plummer softening of length of 10 pc. The time integration is performed using the leapfrog scheme with a variable time step chosen to be 0.05 the dynamical time scale at the center of the halo.

The numerical scheme aims at modeling the dynamical consequences of the following processes:

I. *Gas cooling*: the mass of the cool gas, M_g , is increased linearly from zero to $M_g = f_g M_h$ in the time period from $t_{C1} = 1$ to $t_{C2} = 2$ Gyr. The parameter $f_g = \Omega_b/\Omega_m$ is the gas fraction of the total halo mass. The mass of each collisionless particle is accordingly reduced by a factor $1 - M_g(t)/M_h$. The distribution of the cool mass, $M_g(t)$, is set according to the density profile of the observed stellar profile described below.

II. Trimming/Stripping:

a. *Linear*: Collisionless particles lying at time t beyond a trimming radius $r_{tr}(t)$ are excised from the simulations, where $r_{tr}(t)$ varies linearly from $r_{tr} = r_v$ at $t_{tr1} = t_{C2} = 2$ Gyr to $r_{tr} = 10$ kpc at $t = t_{tr2} = 4$ Gyr.

b. *Dynamical tidal stripping*: the actual gravitational field of the parent halo is included in the simulation. The satellite is assumed to move on a circular orbit and the equations of motion are solved in the non-inertial frame rotating with the satellite, taking into account the Coriolis and centrifugal forces in addition to the gravity of the parent halo. As before, the gravitational force of the satellite is computed assuming spherical symmetry with respect to its centre. The approximation of spherical symmetry is unrealistic for the already stripped particles forming galactic streams. However, the dynamics of those particles is irrelevant to us.

III. Galactic winds:

a. *Fast*: a mass $M_g = f_g M_h - M_*$, where M_* is the observed mass of the stellar component, is suddenly removed from the accreted baryons at $t = t_{w1} = t_{tr2} = 4$ Gyr. The remaining mass M_* is fixed thereafter and represents the observed stellar component.

b. *Slow*: a mass $M_g = f_g M_h - M_*$ is removed linearly with time between $t = t_{w1}$ and $t_{w2} = 8$ Gyr.

For reference, the period of a circular orbit of radius (in kpc) r_{kpc} is $t_c = 2\pi(r_{\text{kpc}}^3/GM)^{1/2} = 0.3(r_{\text{kpc}}^3/M_8)^{1/2}\text{Gyr}$ where M_8 is the mass (in $10^8 M_\odot$) within r_{kpc} . For $M \sim 10^8 M_\odot$ at $r \sim 2$ kpc giving $t_c \sim 0.85$ Gyr for the orbital period of a circular orbit at $r \sim 2$ kpc inside [KKS 2000]04. The circular orbital period in the parent galaxy is $t_c^{\text{DF}2} \sim 2.5(R_{100}/V_{250})$ Gyr, where R_{100} is the orbital radius in 100 kpc and V_{250} is the velocity in 250 km s^{-1} .

The approach outlined above is obviously quite limited in comparison to 3D simulations of galaxy formation, but it has the advantage that the dynamical consequences of the baryonic processes can easily be assessed and discerned. Full 3D simulations including gas process, star formation, and feedback are more realistic, but they suffer from uncertain complex sub-grid modeling and are substantially harder to analyze.

2.2. The stellar density profile

We describe the 3D density distribution of the observed stellar component in terms of an Einasto profile

$$\rho_*^E = \rho_0 \exp \left[- \left(\frac{r}{h} \right)^{1/n} \right], \quad (1)$$

where $n = 0.649$, $h = r_{-2}/(2n)^n$, $r_{-2} = 2.267$ kpc and ρ_0 and ρ_0 is tuned to yield the total mass. This profile yields a good fit to the 2D Sérsic profile representing the observed surface brightness with $R_e = 2$ kpc (for $D = 18$ Mpc) and a Sérsic index $n = 0.6$ (van Dokkum et al. 2018a). The stellar mass is normalized to $1.6 \times 10^8 M_\odot$. The left panel of Fig. 1 plots the Sérsic profile as a function of the projected distance, R , together with the surface density obtained by integrating the Einasto profile along the line of sight out to a maximum 3D radius of 10 kpc. The agreement between the two profiles is excellent. To the right we show the mass enclosed in cylinders of radius R for these two profiles. In addition, we show here the 2D mass obtained with an NFW profile of virial mass $M_h = 10^{10} M_\odot$ and $c = 9$ pruned at a 10 kpc 3D distance.

2.3. Derivation of the stellar velocity dispersion

Our goal is predicting the line of sight velocity dispersion as a function of the projected distances. The simulations provide the total gravitational force field (per unit mass), $g(r)$, resulting from the DM and baryonic components. Since the stellar component is represented in terms of a fixed density profile, we resort to the Jeans equation in order to derive the velocity dispersion of the stars.

Let $\sigma_r^2(r) = \langle v_r^2 \rangle$ be the stellar velocity dispersion in the radial direction at distance r from the center of the galaxy. The velocity anisotropy ellipsoid is described by the parameter $\beta(r) = 1 - \sigma_t^2/2\sigma_r^2$ where $\sigma_t^2 = \sigma_\phi^2 + \sigma_\theta^2$ is the velocity dispersion in the direction tangential to r . The Jeans equation

for a steady-state distribution of stars is

$$\frac{dn\sigma_r^2}{dr} + \frac{2\beta}{r}n\sigma_r^2 = -ng \quad (2)$$

where $n = n(r)$ is the known number density of stars at r . Assuming β is independent of r , the solution to this equation is

$$\sigma_r^2 = -\frac{1}{n(r)r^{2\beta}} \int_r^\infty n(r') r'^{2\beta} g(r') dr'. \quad (3)$$

There is no restriction on β in the expressions above, but there is no guarantee that a particular β actually corresponds to any physical system described by a steady-state phase space distribution function (DF). Indeed, numerical integration of Eddington's formula did not yield a nonnegative isotropic DF (i.e. $\beta = 0$); (see the discussion in §4.3.1 in Binney & Tremaine 2008) that describes the observed stellar distribution (modeled as an Einasto profile) in equilibrium under its self-gravity and the gravity of an NFW halo. For $\beta < -0.01$, models of the form $f(E) = L^{-2\beta} f_1(E)$ are numerically found to be consistent with the desired configuration. We thus restrict ourselves to negative β^2 .

We choose the line of sight to lie in the z -direction. The velocity dispersion, $\sigma_z^2 = \langle v_z^2 \rangle$, at a point R and z is

$$\sigma_z^2 = \sigma_r^2 (1 - \beta \sin^2 \theta), \quad (4)$$

where $\sin \theta = R/\sqrt{R^2 + z^2}$. The observed parallel velocity dispersion at a projected distance R is

$$\sigma_u^2 = \frac{1}{\int_{-\infty}^{\infty} dz n(z, R)} \int_{-\infty}^{\infty} dz n(z, R) \sigma_z^2. \quad (5)$$

Comparing to the observed velocity dispersion, we show (unless stated otherwise) results after averaging σ_u^2 over the stellar surface density within R .

3. RESULTS

The initial mass in stars and cool gas in the progenitor satellite are set to zero, and the initial positions and velocities of the collisionless particles are sampled from an ergodic (i.e. isotropic) phase-space DF. The DF is numerically derived from the NFW density profile by integrating the Eddington relation. This DF is a monotonic function of energy, and thus, the system is stable (Binney & Tremaine 2008). The simulations are run for a period of 9.7 Gyr. In order to reduce effects related to the finite number of particles, the simulations are first run for 1 Gyr, before the sequence of baryonic processes is implemented (I–III above). The energy

² Including only the self-gravity of the stellar component allows for an isotropic and nonnegative DF. But for $\beta > 0$, the models $f(E) = L^{-2\beta} f_1(E)$ lead to negative f .

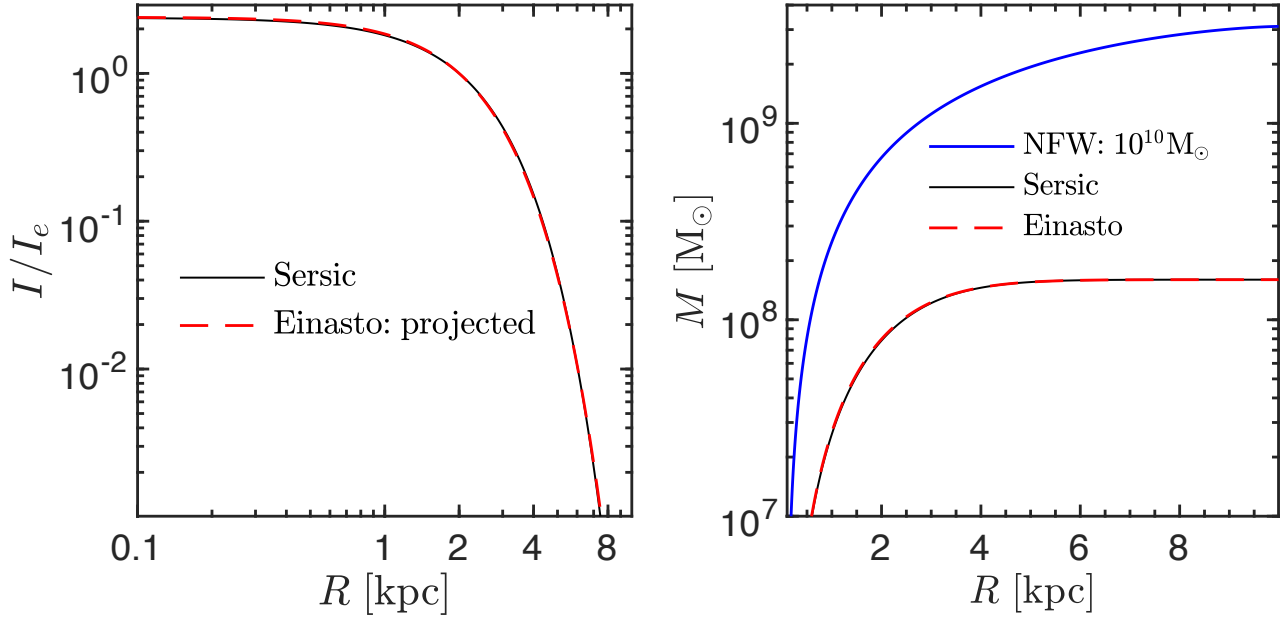


Figure 1. Left panel: the stellar surface density versus projected distance R . The Sérsic fit to the observed [KKS 2000]04 stellar distribution is shown as the solid black line, while the overlapping dashed red line is the projected 3D Einasto profile truncated at 10 kpc. Right panel: stellar mass within 2D cylinders versus R . The solid blue line correspond to an NFW halo with $M_h = 10^{10} M_\odot$ and $c = 9$ truncated at 10 kpc.

conservation of the code for 10^6 self-gravitating collisionless particles alone is better than 1 part in 10^4 .

We will explore the consequences of the processes discussed in §2.1 for halos with NFW density profiles corresponding to virial masses, $M_h = 10^{10} M_\odot$ and $5 \times 10^{10} M_\odot$ at $z = 0$ and $M_h = 2 \cdot 10^{10} M_\odot$ at $z = 2$. The virial radius and circular velocity corresponding to $M_h = 10^{10} M_\odot$ are 46 kpc and 31 km s^{-1} , respectively. For this halo, we consider two values of the concentration parameter, $c = 9$ and 13. Using the Ludlow et al. (2016) recipe for calculating the halo concentration versus halo mass (hereafter, the $c-M$ relation), the mean concentration for halos of this mass is $c = 12.4$. The value $c = 9$ is within the 1σ scatter of the expected variations of c in relaxed halos (see Fig. 5 in Hellwing et al. 2016) and is motivated by the analysis of Nusser (2019), which found that the GC kinematics prefers smaller concentrations. For the larger halo $M_h = 5 \times 10^{10} M_\odot$ we consider $c = 8$ and $c = 11$, where the $c-M$ relation gives $\bar{c} = 11.1$ and $c = 8$ is within the 1σ scatter. The virial radius and the circular velocity of this halo are 78 kpc and 53 km s^{-1} , respectively. The $z = 2$ halo with $M_h = 2 \cdot 10^{10} M_\odot$ actually matches the median mass of the progenitor of the $z = 0$ $M_h = 5 \cdot 10^{10} M_\odot$ halo (Correa, et al. 2015). For the Planck cosmology, the critical density, $\rho_c = 3H_0^2/8\pi G$ is a factor of nine larger at $z = 2$, yielding a virial radius of 28 kpc for $M_h = 2 \cdot 10^{10} M_\odot$ at $z = 2$. Assuming the evolution of the halo is close to stable clustering, the density profile of the $z = 2$ halo should agree with $z = 0$ halo profile at $r < 28$ kpc. Indeed, the mass within a radius of 28 kpc in the large

$z = 0$ halo is $2.4 \cdot 10^{10} M_\odot$, close to the mass of the $z = 2$ halo. According to the recipe of Ludlow et al. (2016), the median concentration of the $z = 2$ halo is $c = 6$. We therefore find $c = 3$ to be the concentration of this halo at which we find consistency with the expected scatter in the $c-M$ relation. The number of collisionless particles in the simulations with the high-mass halo is 10^7 and 10^6 for the two lower-mass halos.

3.1. Small halo

We begin with $M_h = 10^{10} M_\odot$. Using the Jeans equation, we calculate σ_u from the simulation output as described in §2.3. Fig. 2 plots curves of σ_u versus the projected distance R for $c = 9$ (left column) and $c = 13$ (right). Each group of curves corresponds to four values of β , as indicated in the middle row panels. The group of black curves in the top row panels are computed from the simulations at $t = 1$ Gyr (black curves), just before gas cooling is switched on, as described in §2.1. At this stage, neither the stellar nor the cool-gas component have formed, but we still compute σ_u for a population of “massless” tracers distributed according the observed density profile ρ_*^E given in Eq. 1. The diamond and open circle with attached error bars represent the observed velocity dispersions from Danieli et al. (2019) and Emsellem et al. (2018), respectively. These points are plotted at different projected distances as given in those papers. This figure refers to results without any trimming/stripping.

At 2 Gyr (blue curves, top panels), the cooling phase ended with a cool-gas mass $M_g = (\Omega_b/\Omega_m)M_h = 1.55 \times 10^9 M_\odot$

assumed to follow the form ρ_*^E . There is a significant enhancement of σ_u as a result of the transfer of mass from the collisionless particles to the more centrally concentrated baryonic component. During the period 2-4 Gyr, the baryonic component remains the same and since no trimming is invoked, the distribution of the collisionless particles essentially remains the same.

The red curves in middle panel show σ_u just after an event of fast wind ejecting in a single burst a mass $M_g - M_* = 1.39 \times 10^9 M_\odot$ corresponding to all available cool gas after leaving behind the stellar component with $M_* = 1.6 \times 10^8 M_\odot$. In the same panels, the blue curves correspond to a slow wind lasting until $t_{w2} = 8$ Gyr (see III.b in §2.1). Since the slow wind begins at $t_{w2} = 4$ Gyr, the blue curves in the middle and top panels are almost identical, with small differences entirely due to fluctuations in the distribution of the collisionless particles.

By $t = 9.7$ Gyr, the system reaches a steady state with a galaxy made of DM collisionless particles in addition to stellar component of mass M_* . The results for $c = 9$ in the bottom panel on the left indicate that steady state is sensitive to the gas removal mode. The fast wind is more efficient at bringing the velocity dispersion to a comfortable agreement with the observations. As evident in the bottom panel in the column to the right, for the larger concentration, $c = 13$, the final σ_u is consistent with the measured dispersion at about the 2σ level for $\beta = -1$ and $\beta = -1.5$. For this more concentrated halo, the two wind modes yield roughly similar results.

Fig. 3 explores the effect of linear trimming (II.a in §2.1). For brevity, the plot shows the results in the steady state limit at $t = 9.7$ Gyr. Trimming has very little effect on σ_u for the simulations with $c = 9$, as readily seen by comparing this figure and the bottom panel in the previous figure. For $c = 13$, the effect of trimming is more pronounced for the fast wind mode, while almost negligible for slow wind. To understand this behavior, we inspect in Fig. 4 the actual density profile for various cases. The solid and dashed curves in blue ($c = 9$) correspond to densities of DM particles at the final time for untrimmed and trimmed simulation runs, respectively. The curves almost overlap out to $r = 4$ kpc and are below the observed stellar density (dotted cyan) in the range 2-5 kpc. This explains why trimming almost has no effect on σ_u for $c = 9$. Further, the gravitational effects of gas ejection are clearly visible in the DM profile for the untrimmed case at r larger than a few kpc. However, for $c = 13$, the red curves deviate at $r \gtrsim 1$ kpc and both are above the observed stellar density. The same conclusions can be reached from Fig. 5 showing the mass within a radius r . The differences in $M(r)$ between the trimmed and the untrimmed simulations is clearly more pronounced for $c = 13$ (red) than $c = 9$ (blue).

Even for the larger concentration, provided β is sufficiently low, the model curves are consistent with the data at less than the 2σ and 1σ for the [Danieli et al. \(2019\)](#) and [Emsellem et al. \(2018\)](#) points, respectively.

3.2. Large halo

We now turn to the larger halo with $M_h = 5 \times 10^{10} M_\odot$. In this case, the gas mass that can collapse to the inner regions is five times larger than in the $10^{10} M_\odot$ halo. Thus, despite the deeper potential well ($V_c = 52 \text{ km s}^{-1}$ compared to 31 km s^{-1}), the fraction of gas to original DM mass within 10 kpc is actually larger than in the smaller halo, 1.02 versus 0.514 for $M_h = 10^{10} M_\odot$ with $c = 9$.

The results are shown in Fig. 6 for the cool-gas mass fraction, $f_g = M_g/M_h = \Omega_b/\Omega_m = 0.155$ and also for nearly half this value, $f_g = 0.07$. To avoid cluttering of the figure, we show results obtained with $\beta = -1.5$ only and simply point out that at $R \approx 0$, the velocity dispersion for $\beta = -0.01$ is nearly a factor of two larger than $\beta = -1.5$. The cyan solid line corresponds to $c = 11$ falling on the $c-M$ relation ([Ludlow et al. 2016](#)), while all other lines are for $c = 8$. The bottom panel demonstrates that the ejection of the relatively large amount of gas for $f_g = 0.155$ brings down σ_u (dashed-dotted) to a level completely consistent with the observations for $c = 8$. The agreement with the observed σ_u is even better than the corresponding $\beta = -1.5$ curve plotted the bottom panel in Fig. 2 for the lower-mass $M_h = 10^{10} M_\odot$. Like in the the lower mass case, the concentration parameter plays an important role. Comparing between the cyan solid and the red dashed-dotted lines, the velocity dispersion for $c = 11$ is nearly 50% higher than $c = 8$ at $t = 9.7$ Gyr. The following conclusions are also valid for $c = 11$, but for clarity of the figure, we only plot results for $c = 8$. For $f_g = 0.155$, the trimmed and untrimmed simulations yield very similar σ_u . Therefore, only the trimmed results are presented in Fig. 6. In contrast, for $f_g = 0.07$, trimming has a significant effect on the final σ_u as revealed by the comparison between the dotted (trimmed) and dashed (untrimmed) curves in the bottom panel. It is intriguing, however, that the two curves are almost identical at the earlier time, $t = 4$ Gyr, as shown in the middle panel (small differences can be seen by inspecting the actual numerical value). To understand this behavior, we plot in Fig. 7 the density profiles obtained with $f_g = 0.07$. At 4 Gyr, the trimmed (blue dashed) and untrimmed (red solid) almost completely overlap out to $r = 3$ kpc. The red dotted curve shows the baryons (cool gas + stars) density just before ejection by fast wind just before 4 Gyr. Thus, between 1 kpc and 8 kpc the baryons are actually dominant until gas removal.

For $c = 8$, even the smaller f_g (dotted magenta) yields a reasonable agreement with the observations at less than a 2σ deviation from the [Danieli et al. \(2019\)](#) measurement (dia-

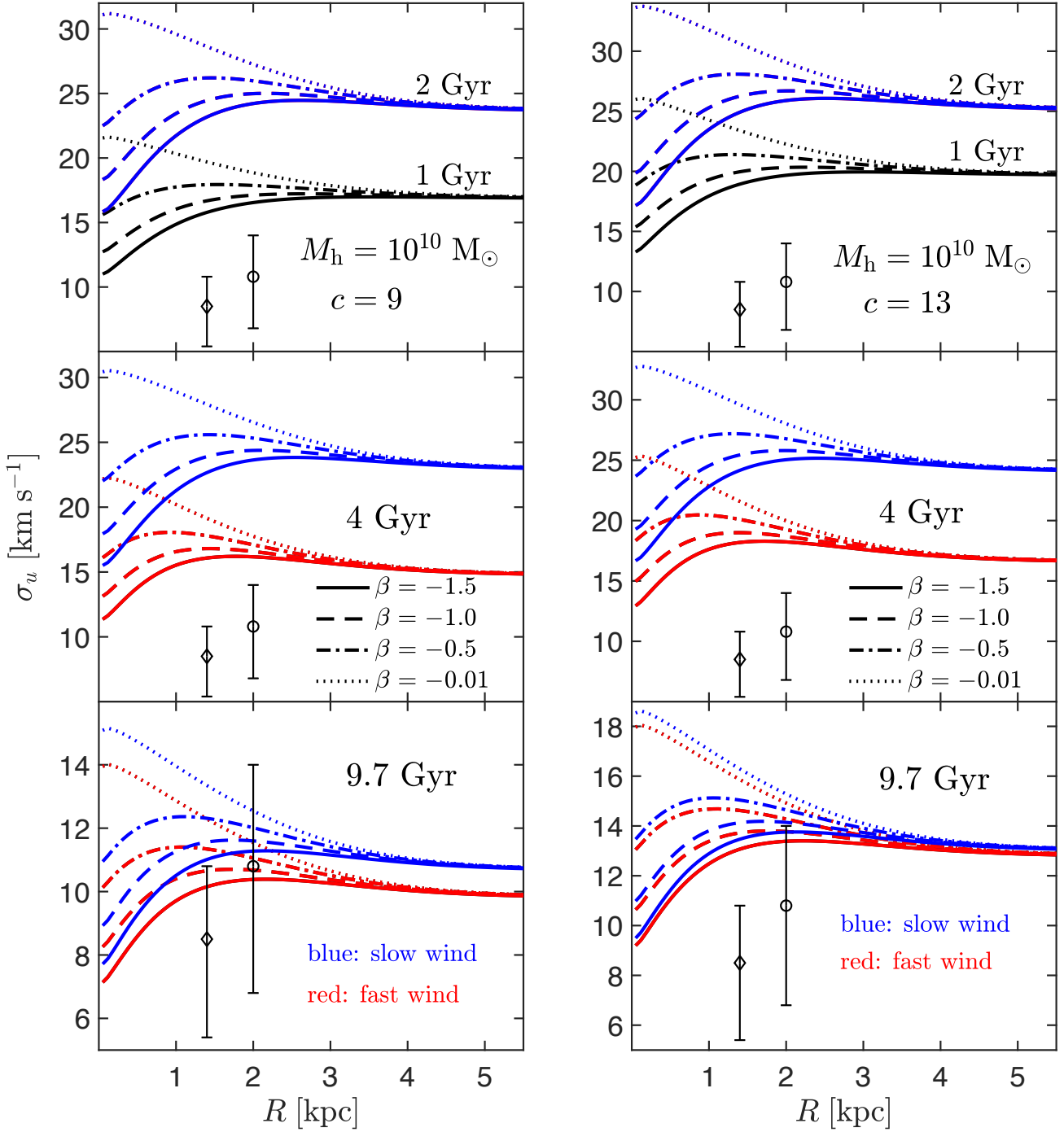


Figure 2. The LOS velocity dispersion versus projected distance obtained from the simulations with virial halo mass $M_h = 10^{10} M_\odot$ and $c = 9$ (column to the left) and $c = 13$ (to the right). Each group of four curves represent four values of the velocity anisotropy parameter, β , as indicated in the middle row. Red and blue correspond to fast and slow winds, respectively. At $t = 2$ Gyr, the red and blue curves overlap. The black curves in the top panel shows results at 1 Gyr just before the gas is collapsed. Shown are results from simulations without tidal stripping/trimming. The diamond and open circle are the (Danieli et al. 2019) and (Emsellem et al. 2018) measurements, respectively. The value $f_g = 0.155$ is assumed.

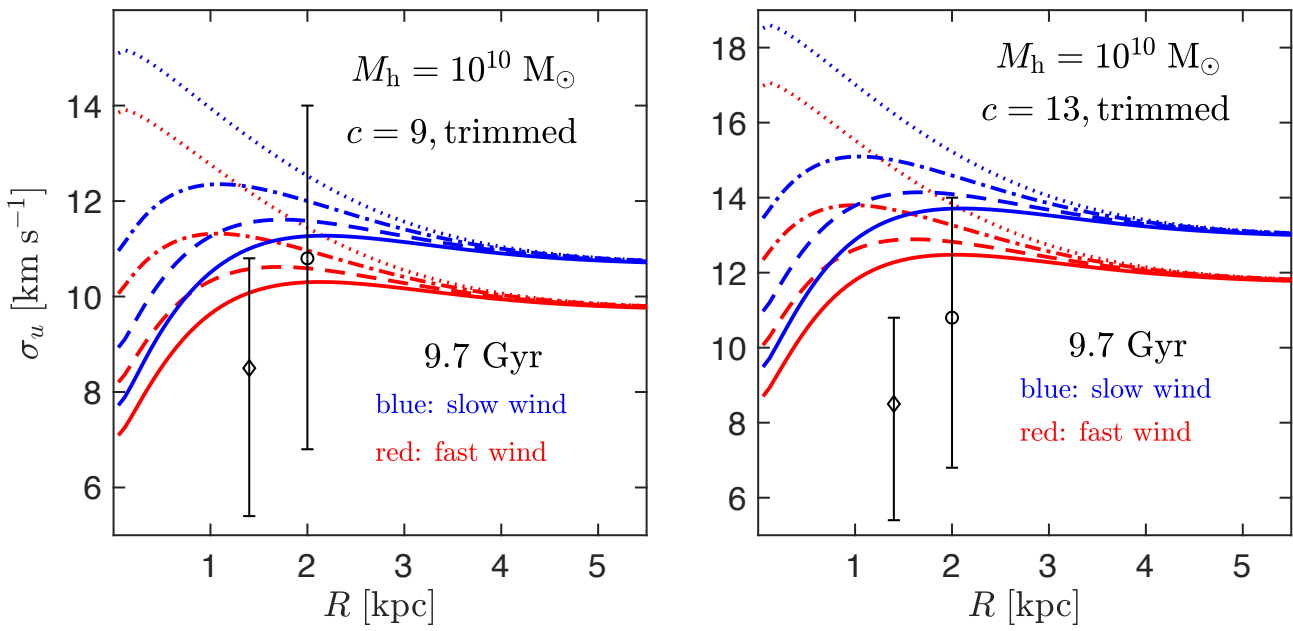


Figure 3. The same as the bottom panels in the previous figure but for the simulations with trimming.

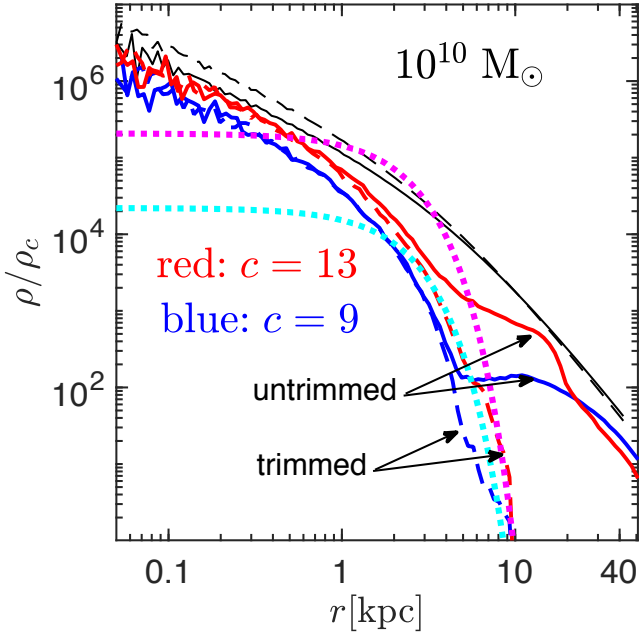


Figure 4. Density profiles (in units of the critical cosmic density) obtained from the simulations with fast wind for $M_h = 10^{10} M_\odot$. Dashed and solid thin black are the DM density profiles, respectively, for $c = 13$ and $c = 9$, at $t = 1$ Gyr just before turning on gas cooling. The DM profiles at $t = 9.7$ Gyr without trimming are thick solid, where the red is for $c = 13$ and blue for $c = 9$. The thick dashed curves are the same as the solid, but for simulations with linear trimming. The dotted blue curve is the stellar profile at the final time, while the dotted red is the baryonic density profile at $t = 2$ Gyr, i.e. the maximum value reached by M_g .

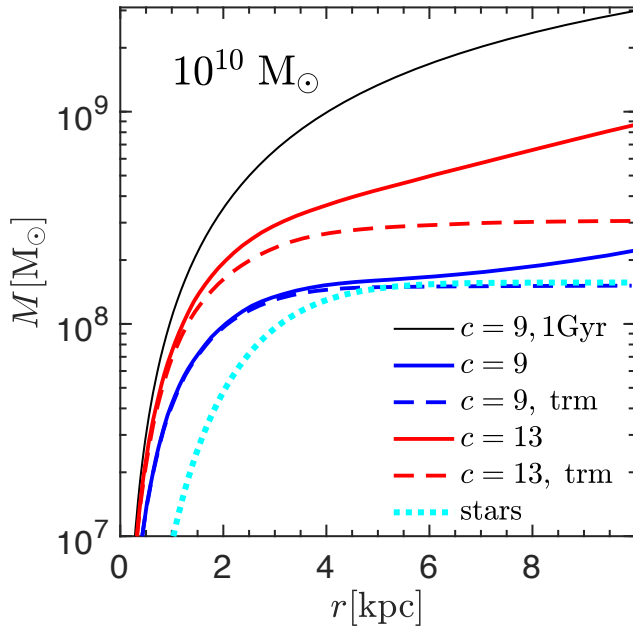


Figure 5. Mass enclosed in a 3D radius r for several of the density profiles from the previous figure.

mond symbol). Note that the at 2 Gyr (top panel), the gas contraction with the larger f_g boosts σ_u to higher values than low f_g . At 9.7 Gyr (bottom panel), the situation is reversed so that the large f_g having lower σ_u . This is due to the more substantial reduction in the total gravity as a result of the removal of a larger amount of gas. For $f_g = 0.07$ and $c = 11$ (not shown), the value of σ_u reaches 14 km s^{-1} at $R \approx 2$.

So far, we have considered the linear trimming recipe III.a in §2.1. It is prudent to explore whether this recipe mimics, at least approximately, a realistic stripping by the gravitational fields of a host halo. For this purpose, we apply the dynamical recipe III.b assuming the satellite moves on a circular orbit of radius 300 kpc in the gravitational field of an NFW host halo of virial mass $2.9 \times 10^{12} M_\odot$ and $c = 8$. We run the simulation for the large-mass case $M_h = 5 \times 10^{10} M_\odot$ with $c = 8$, where the equations of motion are written and numerically solved in the non-inertial frame attached to the satellite. As we already have found for the linear trimming recipes, the corresponding dynamical effects are more pronounced for the low gas fraction $f_g = 0.07$. Hence, the simulation with dynamical trimming is run with this gas fraction. Curves of σ_u from the simulation output at 9.7 Gyr are plotted in red in Fig. 8. Also plotted, in blue, are the results from the linear trimming obtained previously (see Fig. 6). It is reassuring that the two recipes yield similar results but perhaps not surprising since, in both cases, the stripped matter is well outside R_e . Given the approximate nature of the analysis here, we do not make any further attempt to tune the parameters of the host halo in order to bring the dynamical trimming even close to the linear trimming. The agreement seen in the figure is quite satisfactory for our purposes.

3.3. High z Halo

Fig. 9 plots the results for the high z $M_h = 2 \times 10^{10} M_\odot$ halo with linear trimming, in the same format as Fig. 2. Since the mass of the $z = 2$ halo matches the median mass of the progenitor of the $z = 0$ large $M_h = 5 \times 10^{10} M_\odot$ halo, we compare these results with those of Figure 6 for the larger halos. To match the amount of cool gas in the two halos, a fraction $f_g = 0.07$ for the $z = 0$ high-mass halo should be compared with $f_g = 0.155$ for the lower-mass higher z halo. Before the initiation of the baryonic processes at 1 Gyr, we obtain similar σ_u in the high-redshift halo and the $z = 0$ large $M_h = 5 \times 10^{10} M_\odot$ halo. Also, at the 2 Gyr when cooling ends and at the final time, 9.7 Gyr, the corresponding curves in the two halos agree well. Fast wind is more efficient at reducing σ_u . But both modes, fast and slow, agree with the data at a reasonable level. Trimming is important for the high- z halo, as seen in Fig. 10, but σ_u is still consistent with the Emsellem et al. (2018) measurement for the lower β .

3.4. Velocity dispersion at larger distances: The globular clusters

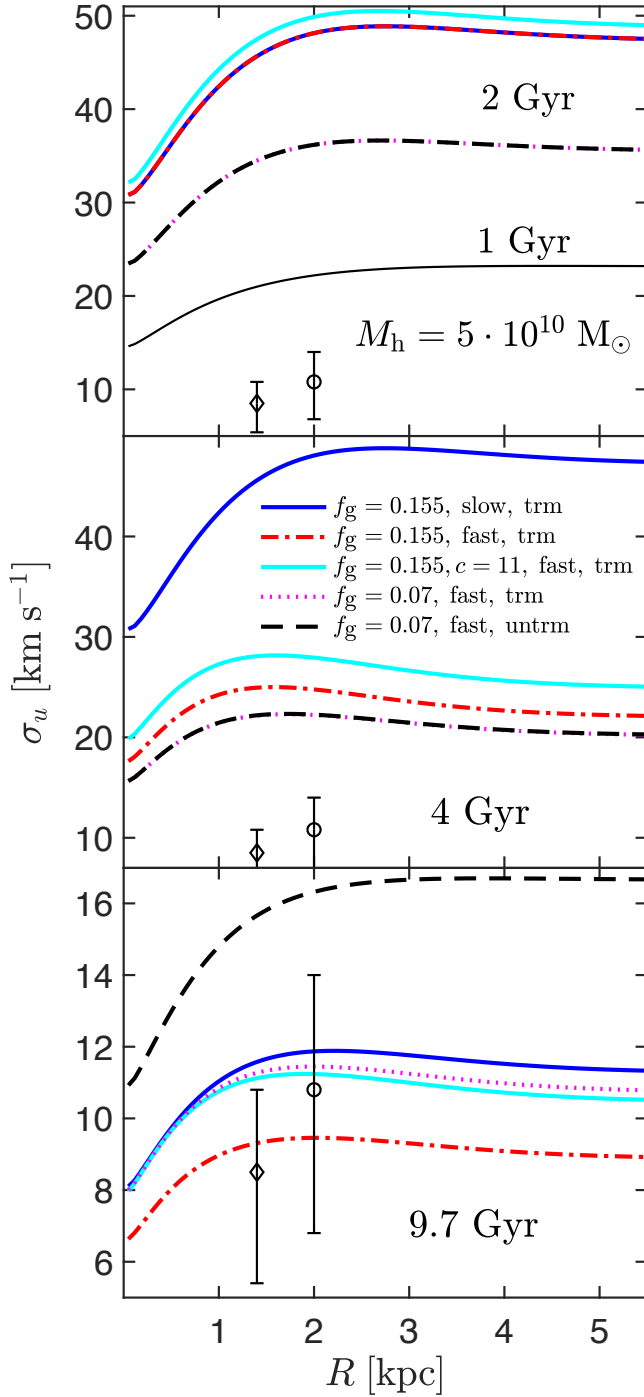


Figure 6. The LOS velocity dispersion from the simulations with $M_h = 5 \times 10^{10} M_\odot$ and $c = 8$, with the exception of the cyan solid line, which is for $c = 11$. Only results for $\beta = -1.5$ are plotted. In the top panel, curves with the same f_g overlap. In the middle panel, just after fast gas ejection at 4 Gyr, despite the trimming, the curves with $f_g = 0.07$ are almost identical, but diverge by 9.7 Gyr as seen in the bottom panel.

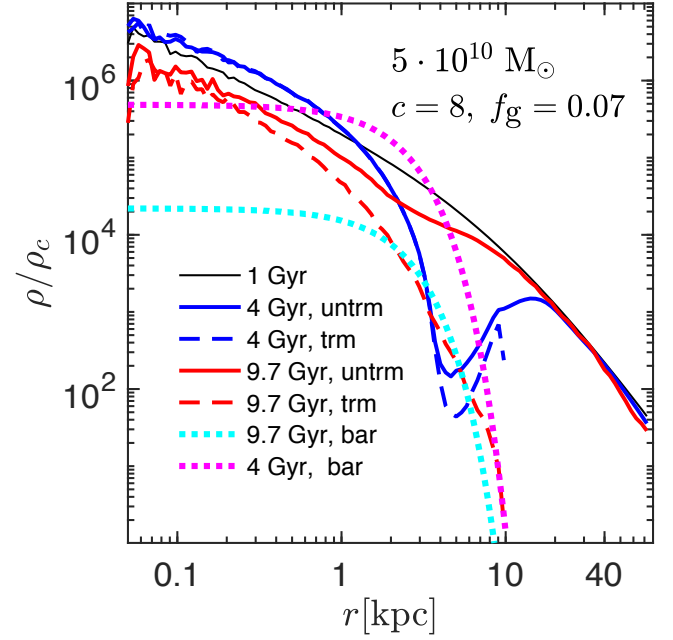


Figure 7. Density profiles from the simulations with $M_h = 5 \times 10^{10} M_\odot$ with $c = 8$ for fast winds. The dotted blue curve is the stellar profile at the final time, while the dotted red is the baryonic density profile at $t = 2$ Gyr, i.e. the maximum value reached by M_g .

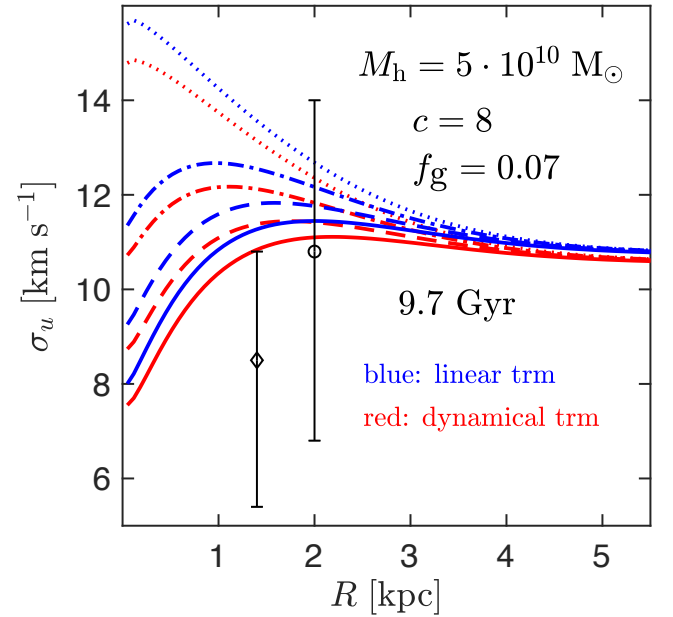


Figure 8. A comparison of the velocity dispersion obtained with linear and dynamical trimming recipes with fast gas removal. The different line-styles refer to different values of β , as in Fig. 2

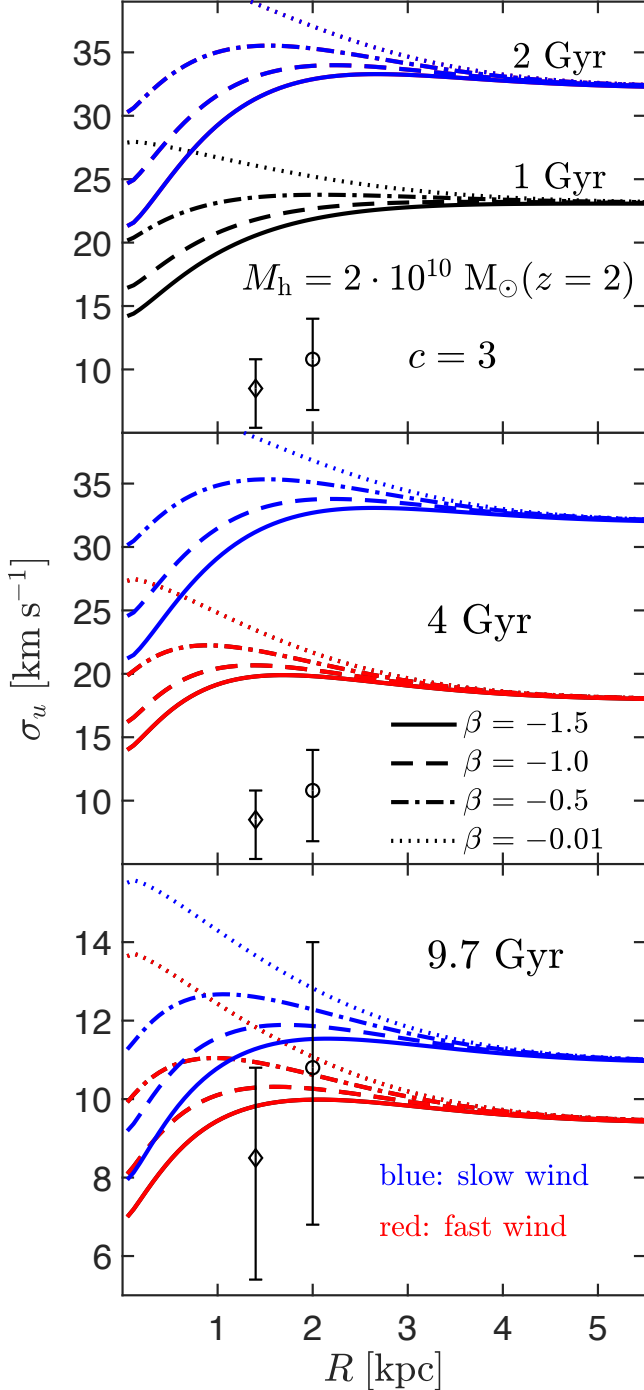


Figure 9. The line of sight velocity dispersion within a projected distance R from the simulations with $M_h = 2 \times 10^{10} M_\odot$ at $z = 2$ including linear trimming at 10 kpc. The value $f_g = 0.155$ is assumed.

We briefly discuss the agreement between the scenario presented here and the kinematical observations of GCs in [KKS 2000]04. For these tracers, individual velocity measurements are available (van Dokkum et al. 2018a). Unfortunately, the number of these tracers is small and the errors are

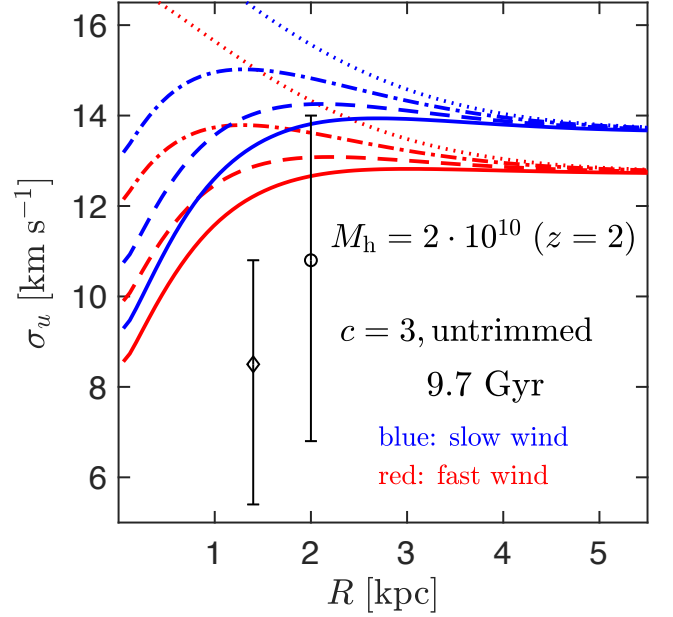


Figure 10. The same as the bottom panel in the previous figure but without trimming of the halo.

large. Nusser (2019) presented an analysis based on the full phase space DF under the assumption of tidal stripping, but without the inclusion of the effects of gas cooling/ejection. We do not intend to apply the DF analysis to the model of the current paper. Instead, we provide a prediction for σ_u and contrast it with the GC measured velocities. This is done in Fig. 11 plotting σ_u obtained as described in §2.3, but with $n \propto r^{-2.3}$ which is consistent with the observed distribution of the GCs on the sky (Nusser 2019; Trujillo et al. 2019). The results are shown for four values of β , as indicated in the figure. Note that here we show predictions for $\beta = 0.5$, since a steady state DF of the form $L^{-2\beta} f_1(E)$ with $\beta = 0.5$ can be found. This is in contrast with the stellar distribution whose form did not allow for a DF of that form with a non-negative β . We do not perform a full statistical analysis, but it is evident that the curves of all plotted values of β are in reasonable agreement with the data.

4. SUMMARY AND CONCLUSIONS

Independent of how ultra-diffuse galaxies form (Dalcanton et al. 1997; Amorisco & Loeb 2016; Di Cintio et al. 2017; Rong et al. 2017), we have outlined steps through which a halo with initial $V_c \lesssim 100 \text{ km s}^{-1}$ can harbor a stellar component with an observed velocity dispersion $\sigma \ll V_c$. The proposed scenario relies on common assumptions regarding galaxy formation that, when combined together, can lead to galaxies with kinematics similar to [KKS 2000]04. The main ingredients are as follows: 1) an initially gas-rich satellite galaxy with a progenitor of a halo of mass $\lesssim 5 \times 10^{10} M_\odot$ at $z = 0$; 2) an initial halo described by

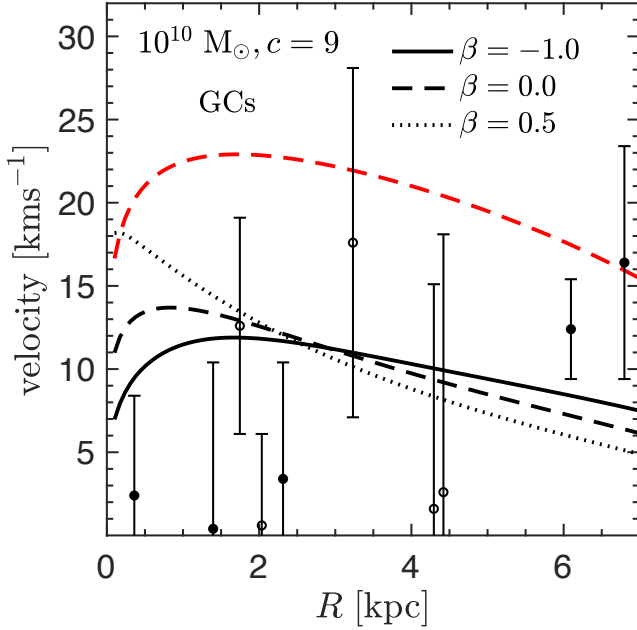


Figure 11. The LOS measured velocities of GCs versus R compared to the predicted σ_u at R (rather than the average within R as in all previous figures). Filled and open circles refer to positive (relative to the mean) and negative GC LOS velocities. The red curve is derived from the initial NFW profile with mass and concentration as indicated in the figure. The black curves are for the final output of the simulation with fast winds and no trimming for $f_g = 0.155$.

an NFW profile with a low concentration ($\gtrsim 1\sigma$ deviation below the mean $c-M$ relation); 3) removal of a significant gas fraction either by SN feedback or/and ram pressure; and 4) stripping of the outer parts of the halo by the external tidal field.

The scenario requires the presence of an initially large cool-gas fraction. This is a reasonable assumption on account of the short cooling time scales. Indeed, for optically selected local galaxies with $5 \lesssim M_*/10^7 M_\odot \lesssim 100$, Papastergis et al. (2012) find HI mass which could easily reach a factor of 10 larger than M_* . The fraction of cool gas at high redshifts, before the bulk of the stars has formed, could be even higher in some galaxies. Measuring the neutral hydrogen fraction is very challenging at high redshift, but the observed large fractions of molecular hydrogen in galaxies at $z \sim 2$ (Tacconi, et al. 2010) implies a large amount of total cool gas as well.

An initially compact stellar component could be puffed-up by the shallowing of the potential well by gas removal. The net outcome would be a diffuse stellar component with very low surface brightness (e.g. Di Cintio et al. 2017). The current work treated the stellar component in terms of a fixed density profile and did not explore this possibility. However, the details of this process in the context of low-velocity-dispersion galaxies, could be tested with simulations, also under the assumption of spherical symmetry, where the stel-

lar component is treated as “live” collisionless particles following a suitable density profile. We leave that for a further study, where the sensitivity to the assumed initial stellar distribution is explored in detail.

It is possible to envisage the formation of completely DM free galaxies through galaxy collisions (Silk 2019) or through the condensation in gaseous debris of galaxy mergers, as in the formation of tidal dwarf galaxies (e.g. Lelli et al. 2015). Both possibilities seem to require fine tuning in order to produce the properties of a galaxy like [KKS 2000]04. In the current paper, we argue that there is nothing grossly unusual in the dynamics of this galaxy and that it is like many other small galaxies that show weak evidence for dark matter. We argue that the low velocity dispersion of [KKS 2000]04 should not serve as an argument for a total lack of dark matter. The [KKS 2000]04 case requires a combination of additional ingredients such as a lower concentration (but still consistent with simulations) and tidal stripping, but all of these are natural in the standard cosmological paradigm.

According to cosmological simulation, low concentrations are generally associated with more extended galaxies according to the relation (Jiang et al. 2019)

$$r_e = 0.02 \left(\frac{10}{c} \right)^{0.7} r_v, \quad (6)$$

where r_e is the stellar half-mass radius. Taking $r_v = 78$ kpc ($M_h = 5 \times 10^{10} M_\odot$), the relation implies 1.45 kpc for $c = 11$, i.e. the mean c for that mass (Ludlow et al. 2016) and 1.8 kpc for $c = 8$. Taking $c = 6$, which is about a 2σ deviation from the mean $c-M$ relation (Hellwing et al. 2016), we get $r_e = 2.23$, compared to the observed $r_e \approx 1.3R_e = 2.6$ kpc. Thus, the lower concentration may also help increase r_e as desired for UDGs.

We have seen that tidal stripping helps lower the velocity dispersion, but but, in contrast to Ogiya (2018) and Carleton, et al. (2018), we do not require an elongated orbit of the satellite inside the host. Instead of bringing the satellite close to the center of the host, we invoke SN feedback and ram pressure. As argued in Nusser (2019), the kinematics of the relative speed between [KKS 2000]04 and the assumed parent galaxy NGC 1052 and the distance between them are likely hard to reconcile with elongated orbits for [KKS 2000]04.

In Nusser (2018), the author showed that orbital decay by dynamical friction of some of the GCs in [KKS 2000]04 is expected. The conclusion was based on simulations that included a dark halo. Dutta Chowdhury et al. (2019) have studied the dynamical friction in this system for the case of no dark matter at all. The presence of a core in the 3D stellar distribution could suppress dynamical friction and even cause buoyancy (e.g. Cole et al. 2012). In addition, scattering among GCs themselves helps keep the GCs afloat around the core at $r \sim 0.3R_e$. A shortcoming of the analysis in

Dutta Chowdhury et al. (2019) is that the GCs are treated as point masses, and therefore, they cannot address the disruptive effects of GC-GC scattering on the GCs themselves. Nonetheless, these authors confirm that dynamical friction is also important (e.g. figures 9 and 10 in their paper). They argue that the observations can be reconciled by starting with a more spatially extended distribution of the GCs, but they do not offer any details of a realistic physical scenario for that setup. The proposal of starting with a more extended GC distribution was also noted in Nusser (2018) as possible solution. The point was originally made by Angus & Diaferio (2009) as a potential solution to the Fornax dynamical friction conundrum (see also Boldrini et al. 2019). A detailed physical formation scenario for this type of initial conditions remains lacking (but see Leung et al. 2020). Thus, despite their conclusion regarding the consistency of the dynamical friction argument with observations, their actual findings actually agree with Nusser (2018).

The scenario presented here requires strong velocity anisotropies with $\beta \lesssim -1$, with clear preference to nearly circular orbits of the stars. This may seem extreme, but the values invoked here are actually favored in several cases (e.g. Chae et al. 2019). More related to the current paper, van Dokkum et al. (2019) find $\beta \approx -1$ from the kinematics

of the UDG Dragonfly 44 under the assumption of NFW profile.

The scenario presented here offers, in principle, a way to prolong dynamical friction timescales. Outward movement of dark matter (of about a few km s^{-1} in the inner few kpc and $\sim 10 \text{ km s}^{-1}$ between 5 and 10 kpc) in response to the reduced gravity due to gas removal could actually result in a reduction in the net sinking rate of GCs to the center. However, a proper quantification of this effect is beyond the scope of the current paper.

We have assumed spherical symmetry without any rotation. Due to the low velocity dispersion of the system, the inclusion of even a mild rotational component (Emsellem et al. 2018) can also substantially boost the inferred mass estimate. (e.g. Nusser 2019; Lewis et al. 2020).

ACKNOWLEDGEMENTS

We thank the anonymous referee for useful comments. This research was supported by the I-CORE Program of the Planning and Budgeting Committee, THE ISRAEL SCIENCE FOUNDATION (grants No. 1829/12 and No. 203/09).

REFERENCES

- Amorisco N. C., Loeb A., 2016, *MNRAS Lett.*, 459, L51
 Angus G. W., Diaferio A., 2009, *MNRAS*, 396, 887
 Auger M. W., Treu T., Bolton A. S., Gavazzi R., Koopmans L. V. E., Marshall P. J., Bundy K., Moustakas L. A., 2009, *ApJ*, 705, 1099
 Behroozi P. S., Conroy C., Wechsler R. H., 2010, *ApJ*, 717, 379
 Behroozi P. S., Wechsler R. H., Conroy C., 2013, *ApJ*, 770, 57
 Binney J., Tremaine S., 2008, *Galactic dynamics*. Princeton University Press
 Boldrini P., Mohayaee R., Silk J., 2019, *MNRAS*, 485, 2546
 Cappellari M., 2016, *ARAAS*, 54, 597
 Carleton T., Cooper M., Kaplinghat M., Errani R., Penarrubia J., 2018, *AAS*, 231, 412.05
 Chae, K.-H., Bernardi, M., & Sheth, R. K. 2019, *ApJ*, 874, 41
 Chowdhury A., 2019, *MNRAS Lett.*, 482, L99
 Cole D. R., Dehnen W., Read J. I., Wilkinson M. I., 2012, *MNRAS*, 426, 601
 Correa C. A., Wyithe J. S. B., Schaye J., Duffy A. R., 2015, *MNRAS*, 450, 1521
 Dalcanton J. J., Spergel D. N., Summers F. J., 1997, *ApJ*, 482, 659
 Danieli S., van Dokkum P., Conroy C., Abraham R., Romanowsky A. J., 2019, *ApJ*, 874, L12
 Danieli S., van Dokkum P., Abraham R., Conroy C., Dolphin A. E., Romanowsky A. J., 2019, arXiv, arXiv:1910.07529
 Dekel A., Silk J., 1986, *ApJ*, 303, 39
 Dekel A., Stoehr F., Mamon G. A., Cox T. J., Novak G. S., Primack J. R., 2005, *Natur*, 437, 707
 Dekel A., Woo J., 2003, *MNRAS*, 344, 1131
 Di Cintio A., Brook C. B., Dutton A. A., Macciò A. V., Obreja A., Dekel A., 2017, *MNRAS*, 466, L1
 Dutta Chowdhury D., van den Bosch F. C., van Dokkum P., 2019, *ApJ*, 877, 133
 Dutton A. A., Maccio A. V., 2014, *MNRAS*, 441, 3359
 Dutton A. A., et al., 2016, *MNRAS*, 461, 1
 Emsellem E., et al., 2018, *A&A*, 625, A76
 Garrison-Kimmel, S., Wetzel, A., Hopkins, P. F., et al. 2019, *MNRAS*, 489, 4574
 Forbes D. A., Sinpetru L., Savorgnan G., Romanowsky A. J., Usher C., Brodie J., 2017, *MNRAS*, 464, 4611
 Hellwing W. A., Frenk C. S., Cautun M., Bose S., Helly J., Jenkins A., Sawala T., Cytowski M., 2016, *MNRAS*, 457, 3492
 Jiang, F., Dekel, A., Kneller, O., et al. 2019, *MNRAS*, 488, 4801
 Muratov A. L., Kereš D., Faucher-Giguère C.-A., Hopkins P. F., Quataert E., Murray N., 2015, *MNRAS*, 454, 2691
 Larson R. B., 1974, *MNRAS*, 169, 229
 Lelli F., et al., 2015, *A&A*, 584, 113L
 Leung, G. Y. C., Leaman, R., van de Ven, G., et al. 2020, *MNRAS*, 493, 320

- Lewis, G. F., Brewer, B. J., & Wan, Z. 2020, *MNRAS*, 491, L1
- Ludlow A. D., Bose S., Angulo R. E., Wang L., Hellwing W. A., Navarro J. F., Cole S., Frenk C. S., 2016, *MNRAS*, 460, 1214
- Mamon G. A., Łokas E. L., 2005a, *MNRAS*, 362, 95
- Mamon G. A., Łokas E. L., 2005b, *MNRAS*, 363, 705
- Martig M., Bournaud F., 2008, *MNRAS Lett.*, 385, L38
- Martin, G., Kaviraj, S., Laigle, C., et al. 2019, *MNRAS*, 485, 796
- Moster B. P., Naab T., White S. D. M., 2013, *MNRAS*, 428, 3121
- Munshi F., et al., 2013, *ApJ*, 766
- Navarro J. F., Frenk C. S., White S. D. M., 1996, *ApJ*, 462, 563
- Nusser A., 2018, *ApJL*, 863, L17
- Nusser A., 2019, *MNRAS*, 484, 510
- Ogiya G., 2018, *MNRAS*, 480, L106
- Padmanabhan N., et al., 2004, *New Astron.*, 9, 329
- Papastergis E., Cattaneo A., Huang S., Giovanelli R., Haynes M. P., 2012, *ApJ*, 759, 138
- Planck Collaboration et al., 2018, eprint arXiv, 1807.06209
- Pontzen A., Governato F., 2012, *MNRAS*, 421, 3464
- Renaud F., Bournaud F., Kraljic K., Duc P.-A., 2014, *MNRAS: Lett*, 442, 33
- Rodríguez-Puebla A., Primack J. R., Avila-Reese V., Faber S. M., 2017, *MNRAS*, 470, 651
- Romanowsky A. J., Douglas N. G., Arnaboldi M., Kuijken K., Merrifield M. R., Napolitano N. R., Capaccioli M., Freeman K. C., 2003, *Science (80-.)*, 301, 1696
- Rong, Y., Guo, Q., Gao, L., et al. 2017, *MNRAS*, 470, 4231
- Sardone A., Pisano D. J., Burke-Spolaor S., Mascoop J. L., Pol N., 2019, *ApJ*, 871, L31
- Silk J., 2019, *MNRAS Lett.*, 488, L24
- Tacconi L. J., et al., 2010, *Natur*, 463, 781
- Thomas J., et al., 2011, *MNRAS*, 415, 545
- Treu T., Koopmans L. V. E., 2004, *ApJ*, 611, 739
- Trujillo I., et al., 2019, *MNRAS*, 486, 1192
- Wasserman A., Romanowsky A. J., Brodie J., van Dokkum P., Conroy C., Abraham R., Cohen Y., Danieli S., 2018, *ApJL*, 863, L15
- White S. D. M., 1983, *ApJ*, 274, 53
- White S. D. M., Frenk C. S., 1991, *ApJ*, 379, 52
- van Dokkum P., et al., 2018a, *Nature*, 555, 629
- van Dokkum P., Danieli S., Cohen Y., Romanowsky A. J., Conroy C., 2018b, *ApJ*, 864, L18
- van Dokkum P., Danieli S., Abraham R., Conroy C., Romanowsky A. J., 2019, *ApJ*, 874, L5
- van Dokkum, P., Wasserman, A., Danieli, S., et al. 2019, *ApJ*, 880, 91